https://doi.org/10.5194/egusphere-2026-5268
Preprint. Discussion started: 9 November 2026
© Author(s) 2026. CC BY 4.0 License.

Effects of brine and gas inclusions on the macro- and microscopic mechanical behaviour of sea ice under bending

Qingkai Wang, Jinpei Li, Kunsen Liu, Zhixing Li, Peng Lu, Zhijun Li

State Key Laboratory of Coastal and Offshore Engineering, Dalian University of Technology, Dalian, 116024, China

Correspondence to: Qingkai Wang (wangqingkai@dlut.edu.cn)

Abstract. The macroscopic mechanical properties of sea ice in flexure are controlled by underlying microstructural damage. In this study, the macro- and microscopic mechanical behaviours of sea ice under four-point bending were investigated using columnar-ice specimens machined from a sea ice block collected in the summer Arctic. Due to brine drainage, the gas content of the specimens exceeded the brine content. A total of 83 bending tests were performed at different temperatures to measure the flexural strength and effective elastic modulus. At each temperature, one specimen was monitored by four acoustic emission (AE) sensors to trace the evolution of microcracking. The flexural strength ranged from 124.6 to 1394.7 kPa, and the effective elastic modulus varied from 0.5 to 4.2 GPa. Both strength and modulus decreased with increasing temperature and gas volume fraction. To extend the range of brine and gas contents, the present data were combined with previous studies, and a two-variable empirical equation was established to estimate sea ice flexural strength using brine and gas volume fractions, unlike conventional formulae based solely on brine content. AE monitoring showed that microcracking activity remained weak before main crack initiation, with low ring-down count and energy. A high-energy AE event triggered unstable propagation of the main crack, leading to the catastrophic failure of ice specimens, rather than a progressive accumulation of microcrack density. Fast Fourier Transform of the AE waveforms identified two typical frequency modes centred at 38 and 150 kHz, corresponding to secondary cracking activity and main crack nucleation, respectively. Compared with freshwater ice, sea ice exhibited more active secondary cracking with larger size, which stems from the inherent brine inclusions that promote discontinuous crack propagation, frictional sliding of crack faces, and tortuous crack paths. These results provide a multiscale understanding of sea ice failure under bending and highlight the influence of sea ice inclusions from a mesoscopic perspective.

1 Introduction

The flexural strength of sea ice is a critical parameter for the design of engineering structures in ice-covered waters. It is also a fundamental property governing sea ice dynamics, influencing the fracture and ridging of the ice cover. The flexural behaviour of sea ice depends strongly on ice temperature, ice type, and the presence of brine and gas inclusions (Timco and Weeks, 2010).

Two main types of tests are commonly used to measure the flexural strength and effective elastic modulus of sea ice: simple beam test and the cantilever beam test. The simple beam test (three- or four-point supported) typically adopts cuboid specimens

https://doi.org/10.5194/egusphere-2026-5268
Preprint. Discussion started: 9 November 2026
© Author(s) 2026. CC BY 4.0 License.

cut from the ice cover, whereas the cantilever beam test is a full-scale measurement performed on an ice beam with the full thickness. Compared with three-point bending, four-point bending provides a wider central region of constant moment and zero shear between the loading points, allowing the beam to fail at the weakest section. The cantilever beam test yields the in-situ flexural strength, but preparing full-thickness cantilever beams is time- and labour-intensive. Using these methods, extensive measurements of sea ice flexural strength have been conducted (e.g., Barrette, 2011; Blanchet et al., 1997; Edington et al., 2025). Additionally, full-scale simple beam tests on sea ice have also been attempted (Karulina et al. 2019; Taylor et al., 2021). Aly et al. (2019) assembled sea ice beam tests to investigate size effects and found a considerable decrease in flexural strength with increasing specimen size. Timco and O'Brien (1994) compiled 939 flexural strength measurements from polar and temperate regions, and proposed a widely used empirical formula of sea ice flexural strength that relies on brine volume fraction. Although this formula has been widely adopted, its applicability is limited to sea ice in the growth season. For melting sea ice, substantial brine drainage occurs and the drained brine channels become occupied by gas, resulting in a high total porosity and low actual strength (Timco and Weeks, 2010). Under such a condition, the formula based on brine content overestimates the strength.

The macroscopic failure of ice is essentially the expression of damage evolution at the microscopic level. In the absence of inclusions and preexisting cracks, crack nucleation in polycrystalline ice is primarily induced by grain boundary sliding (Frost, 2001). In saline ice, the presence of microscopic heterogeneities such as brine inclusions and gas bubbles further amplifies stress concentrations, making them preferential sites for crack nucleation (Picu et al., 1994). Once nucleated, cracks in freshwater ice propagate at speeds of hundreds of meters per second after initiation (Petrenko and Gluschenkov, 1996). In contrast, in saline ice, interactions between cracks and brine inclusions (Arakawa and Petrenko, 2003) reduce the propagation speed to about 10 $m \cdot s^{-1}$ (Petrenko and Gluschenkov, 1996). These microscopic cracking dictate the macroscopic mechanical response of ice. For instance, under unconfined compression, damage accumulates through the stable growth and linkage of wing cracks, ultimately coalescing into axial splitting parallel to the loading direction (Schulson, 2001). As confining pressure increases, cracking becomes suppressed, and the macroscopic failure mode transitions to shear faulting (Schulson, 2001) or transgranular instability (Kolari, 2019).

Acoustic emission (AE) testing is a widely used non-destructive technique for monitoring crack evolution in materials such as rocks (Moradian et al., 2016) and concrete (Ohno and Ohtsu, 2010). AE refers to the phenomenon where elastic waves are released within a medium by damage processes such as crack propagation, plastic deformation, and frictional sliding. Gold (1960) pioneered the application of AE technique to monitor microcrack evolution in ice, but its subsequent use in ice has remained rather limited. Sinha (1982) observed detectable AE signals prior to visible crack formation during the compression of columnar ice, and Weiss and Grasso (1997) used AE techniques to investigate dislocation dynamics during the creep deformation of single crystals in freshwater ice. Li and Du (2016) and Datt et al. (2020) monitored uniaxial compression and three-point bending tests on freshwater ice using AE parameters including amplitude, energy, and b-values. Lishman et al. (2020) conducted field AE measurements on sea ice and suggested that AE techniques can be used to infer damage and healing processes in natural sea ice. Despite these advances, the majority of AE studies on ice have focused on freshwater ice, whereas

https://doi.org/10.5194/egusphere-2026-5268
Preprint. Discussion started: 9 November 2026
© Author(s) 2026. CC BY 4.0 License.

investigations on natural sea ice, which contains multiphase brine and gas inclusions, remain very limited. These inclusions are known to influence microcracking activity (Arakawa and Petrenko, 2003; Petrenko and Gluschenkov, 1996; Picu et al., 1994), yet their effects on AE signatures in sea ice are still poorly understood. Our recent study (Wang et al., 2026) used AE techniques to examine microcracking activity in natural saline ice under uniaxial compression at low strain rates and identified four microcrack-evolution stages. That study established an AE-based framework for characterizing microcrack activity in natural saline ice through AE parameters, b-value analysis and 3D source localization. Building on this methodological framework, the present study extends the investigation to the brittle flexural failure of sea ice, with particular attention to how brine and gas inclusions govern microcracking activity and the associated AE signatures.

To investigate the macroscopic mechanical properties and microscopic crack evolution of sea ice under flexural loading, four-point bending tests were conducted on sea ice specimens in a cold laboratory, with AE monitoring employed to track internal microcracking activity. The relationships of sea ice flexural strength and effective elastic modulus with the inclusion content were quantified, and the characteristic patterns of AE parameters during the bending process were identified. The results will help to deepen the understanding of the multiscale mechanical behaviour of sea ice under bending.

2 Method

2.1 Ice sampling

The ice specimens used in the laboratory experiments were obtained from natural Arctic sea ice. On 15 August 2023, a full-thickness ice block with a thickness of 1.2 m was extracted from level ice in the central Arctic Ocean (84.4 °N, 154.3 °E). The sampling area was free of melt ponds and ice ridges, and the air temperature at the time of sampling was −0.4 °C. After the ice block was retrieved, additional ice cores were drilled in its vicinity for observations of ice temperature and texture. The temperature profiles were measured by inserting a thermometer (accuracy ±0.1 °C) into holes drilled to the core centre at 10-cm intervals along the core length. The ice temperature decreased approximately linearly from the surface to the bottom (Fig. 1a), with an average of −0.9 °C. Thin sections were prepared in vertical direction with respect to the ice surface for crystal structure observations under crossed polarized light. As shown in Fig. 1b, the upper 10 cm of the ice consisted of granular ice, underlain by columnar ice.

https://doi.org/10.5194/egusphere-2026-5268
Preprint. Discussion started: 9 November 2026
© Author(s) 2026. CC BY 4.0 License.

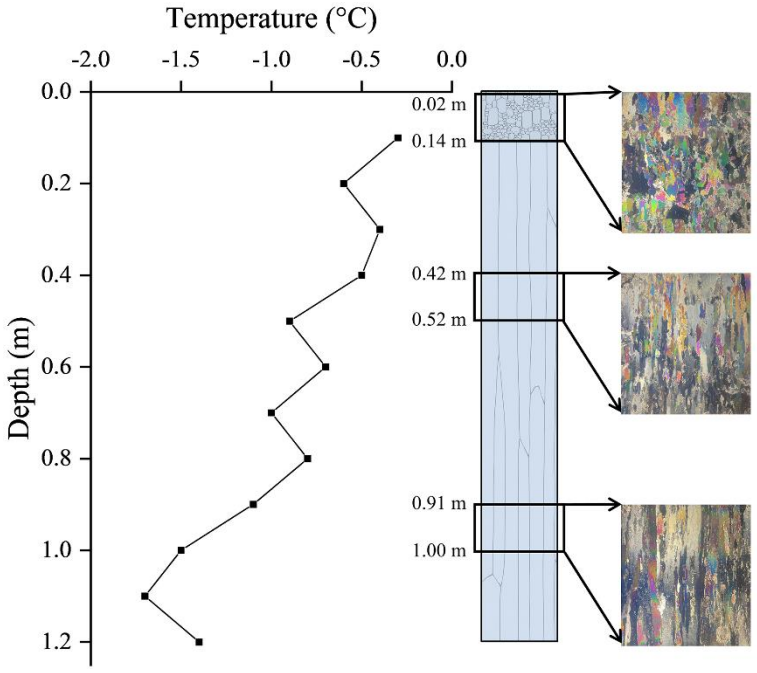


Figure 1: The vertical profiles of the ice: (a) temperature and (b) crystal structure.

The retrieved ice block was cut into several large pieces, stored in insulated containers, and kept at a low temperature throughout transportation to the domestic cold laboratory for subsequent mechanical testing. It is acknowledged that the prolonged transportation had altered the phase composition within the sea ice, particularly leading to brine loss. Consequently, our objective was not to measure the mechanical behaviour of the sea ice in its original in-situ physical state, but rather to characterize its behaviour under well-defined laboratory conditions.

Rectangular beam specimens were prepared from the columnar-ice part of the ice block for the mechanical experiments. The long axis of each specimen was parallel to the original ice surface. A band saw was first used to cut the specimens to a cross-section of 7 cm × 7 cm, and the length was then trimmed to 50 cm. The perpendicularity of the two sides of the cross-section and the horizontality of the long axis was verified using a square ruler. After machining, the specimens were stored in a thermotank (±0.1 ℃) at the target test temperature for at least 24 h.

2.2 Bending test

A total of 83 four-point bending tests were conducted to measure the flexural strength and effective elastic modulus of the specimens. The bending tests were performed using a universal testing machine (Fig. 2) equipped with four welded steel support columns (3 cm in diameter) and a servo motor, which enabled loading at a constant crosshead speed with an accuracy of ±0.25 $\mu m \cdot s^{-1}$. The four-point bending configuration is illustrated in Fig. 3. The supported span (distance between the two supports) was 45 cm, and the loading span (distance between the two loading points) was 15 cm, both arranged symmetrically about the midpoint of the specimen. A load cell with a capacity of 2 kN and an accuracy of ±0.05% was used to measure the

https://doi.org/10.5194/egusphere-2026-5268
Preprint. Discussion started: 9 November 2026
© Author(s) 2026. CC BY 4.0 License.

applied force. Two linear variable differential transformers (LVDTs) with a capacity of 10 mm and an accuracy of ±0.01 mm were symmetrically attached to the bottom surface of the specimen at the midspan to measure the midspan displacement, each positioned 2 cm away from the centre. Both force and displacement were recorded at 100 Hz. The bending tests were conducted at temperatures of −3, −6, −9, and −12 °C with the crosshead speed set to 0.1 $m \cdot s^{-1}$. The failure time of the specimens ranged from 4 to 10 s, which is consistent with the typical failure times reported by Timco and Weeks (2010). The test machine was housed in the cold laboratory where the ambient temperature was maintained to match the specimen storage temperature, with fluctuations of ±0.5 ℃. Before loading, the mass of each specimen was weighted using a balance (±0.1 g), and the volume was calculated based on the dimensions measured using a calliper (±0.02 mm). After failure, each specimen was melted to measure salinity using a salinometer (±0.1 PSU). The brine and gas volume fractions of the specimens were determined using the equations proposed by Cox and Weeks (1983).

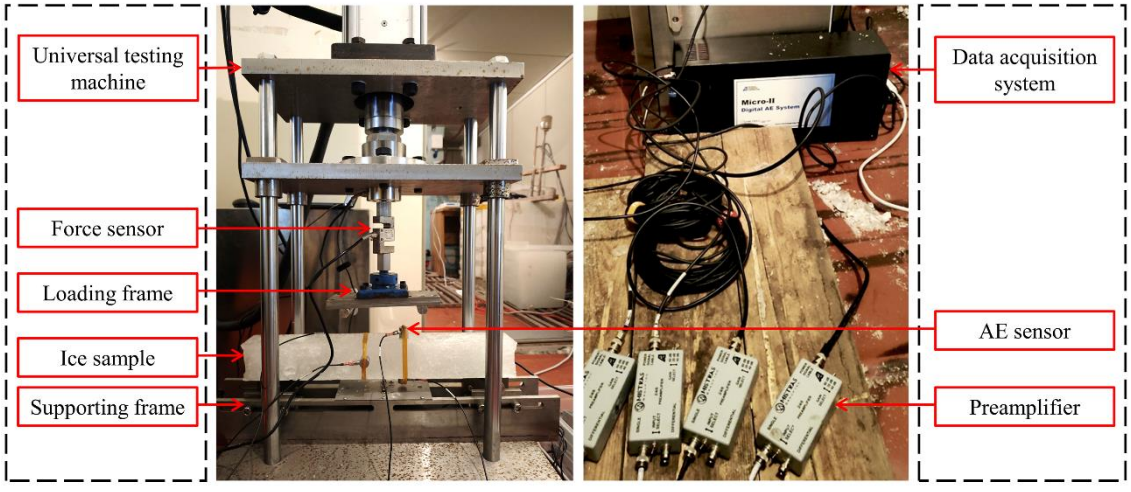


Figure 2: The loading configuration and set up for bending and AE tests.

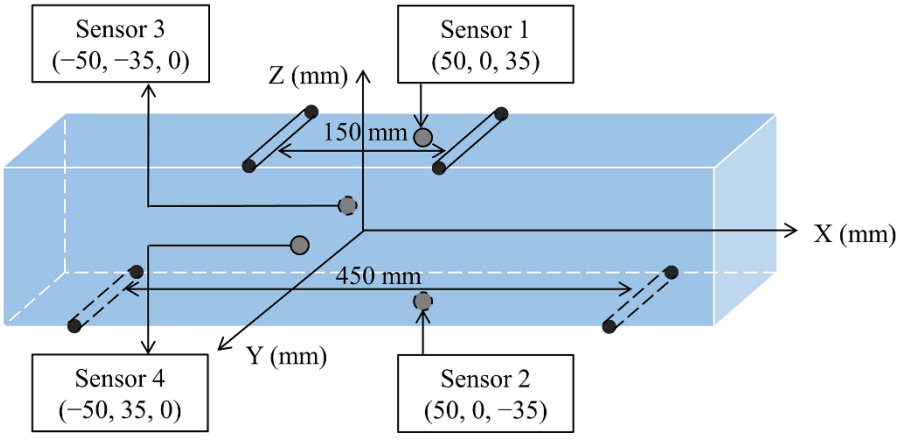


Figure 3: The four-point bending configuration. The coordinates indicate the positions of the AE sensors.

https://doi.org/10.5194/egusphere-2026-5268
Preprint. Discussion started: 9 November 2026
© Author(s) 2026. CC BY 4.0 License.

Based on linear elastic theory, the flexural strength and effective elastic modulus of sea ice under four-point bending are calculated using Eqs. (1) and (2).

$$\sigma_f = \frac{Fl}{bh^2} \tag{1}$$

$$E = \frac{23Fl^3}{108\delta bh^3} \tag{2}$$

where σ_f is the flexural strength, E is the effective elastic modulus, F and δ are the force and midspan displacement at failure, respectively, l is the span between supports, b and h are section width and height of the specimen, respectively.

2.3 AE test

One specimen was selected at each temperature for AE monitoring to characterize microcracking activity during four-point bending. The specimen tested at −9 °C was excluded from the AE analysis because the wave velocities measured in two orthogonal directions differed substantially. The information on the specimens used for AE analysis is given in Table 1.

Table 1: Information on the specimens used for AE tests.

Specimen ID	Temperature (℃)	Salinity (PSU)	Density (kg/m^3)	Brine volume fraction (%)	Gas volume fraction (%)
F1	−3	2.7	849	4.0	8.0
F2	−6	3.1	863	2.4	6.4
F3	−12	1.8	852	0.8	7.5

AE monitoring was performed using a PCI-2 system (Physical Acoustics Corporation), consisting of a data acquisition unit, preamplifiers, and AE sensors (Fig. 2). Given the microstructural heterogeneity of sea ice, the AE acquisition parameters were set according to recommended values for composite materials (Table 2), which follow those used in our previous compression study (Wang et al., 2026) to ensure methodological comparability; the sensor layout, specimen geometry, coupling arrangement and loading fixture were, however, redesigned for the four-point bending configuration (Figs. 2 and 3). Four AE sensors with a centre frequency of 150 kHz and a bandwidth of 50–200 kHz were mounted on individual surfaces of each ice specimen. The frequency range covers the frequency bands of AE signals in ice reported in previous studies (Li and Du, 2016; Lishman et al., 2020). Sensors 1 and 2 were symmetrically attached to the top and bottom surfaces, and sensors 3 and 4 to the front and back surfaces, all at a cross-section located 5 cm from the specimen centre. Silicone grease was applied between the sensor faces and the specimen surface to ensure acoustic coupling, with sensors secured by thin rubber bands with a circumference similar to that of the specimen cross-section. The sensor coupling integrity was verified using the pencil lead

https://doi.org/10.5194/egusphere-2026-5268
Preprint. Discussion started: 9 November 2026
© Author(s) 2026. CC BY 4.0 License.

break method recommended by AE testing industry standard of ASTM E1316–25 (ASTM International, 2025), and the amplitudes from all four channels exceeded 90 dB, indicating satisfactory coupling. In addition, the wave velocities between sensors 1 and 2, and between sensors 1 and 3 on the specimen surface were measured before AE testing using the built-in function of the PCI-2 system. Ambient noise monitoring showed that the background noise was generally below 40 dB; therefore, the detection threshold was set to 40 dB with a floating threshold width of 5 dB. The preamplifier gain was set to 40 dB.

Table 2: The AE acquisition parameters.

Parameter	Value	Parameter	Value
Sampling rate (MHz)	1	Hit lockout time (μs)	300
Length	2048	Event definition value (μs)	300
Pre-trigger (μs)	256	Event lockout value (μs)	500
Peak definition time (μs)	50	Overcall value (μs)	75
Hit definition time (μs)	200		

2.4 AE signal process

The following parameters were extracted from the AE signals for analysis including ring-down count, amplitude, energy, b-value, peak frequency, and centroid frequency.

The ring-down count is the number of times the AE signal exceeds a pre-set threshold during a selected portion of the test.

The AE amplitude is defined as the peak amplitude (in dB) of the waveform within a single AE event, reflecting the instantaneous intensity of the elastic waves released by cracking. It is given by Eq. (3).

$$A = 20\lg\frac{V_{\max}}{V_{\text{ref}}} - P \tag{3}$$

where A is the amplitude, $V_{\max}$ is the maximum transient voltage, V_{ref} is the reference voltage (typically 1 μV), P is the preamplifier gain (set to 40 dB in this study).

The AE energy quantifies the energy released by an emission event, measured in attojoules (aJ = 10^{-18} J), and is calculated using Eq. (4).

$$U = \frac{1}{10\text{k}\Omega}\int_{t_f}^{t_l}\left[V(t)^2\right]dt \tag{4}$$

where U is the energy, $V(t)$ is the voltage corresponding to transient stress wave, t_f and t_l are the times of the first and last threshold crossings, respectively.

https://doi.org/10.5194/egusphere-2026-5268
Preprint. Discussion started: 9 November 2026
© Author(s) 2026. CC BY 4.0 License.

The b-value reflects the ratios of low-amplitude events to high-amplitude events, and is commonly determined using Eq. (5). According to Eq. (5), a higher b-value corresponds to damage dominated by smaller-scale events, whereas a lower b-value indicates that larger-scale microcrack is dominate.

$$b = \frac{20 \times \lg e}{(< A > - A_{\min})} \tag{5}$$

where <*A*> is the average AE amplitude and A_{min} is the minimum amplitude within the calculation window. Following the recommendations of Liu et al. (2020) and Roberts et al. (2015), each calculation window contained 200 AE events.

The peak frequency and centroid frequency were determined from the frequency spectrum obtained by applying a Fast Fourier Transform (FFT) to the AE waveforms. The peak frequency was taken as the frequency corresponding to the maximum spectral amplitude, and the centroid frequency was calculated as the amplitude-weighted average of all frequency components in the spectrum.

2.5 AE source location

The three-dimensional (3D) location of AE sources is essential for analysing microcrack evolution within ice specimens. The location of microcracks is based on the following assumptions (Boniface et al., 2020): (i) AE sources are treated as point sources; (ii) sources are temporally separated, so that the acoustic activity from one event does not overlap with that from another; and (iii) the wave propagation velocity is constant.

In this study, the localization of microcracks was performed using the time difference of arrival (TDOA) algorithm following Wang et al. (2026), and the formulation is reproduced here for completeness. When an AE event is detected by the four non-coplanar sensors used in the test, its source location can be determined as follows. First, the distance *d* from a sensor to the AE source is determined using Eq. (6).

$$d = v \cdot (t - t_0) \tag{6}$$

where *t* and t_0 are the arrival and generation moments, respectively, and *v* is the average acoustic wave velocity obtained using the AST function for each specimen.

Subsequently, the distance from the AE source to *i*-th triggered sensor P_i (*i* = 1–4) is

$$d_i = \sqrt{(x_i - x_s)^2 + (y_i - y_s)^2 + (z_i - z_s)^2} \tag{7}$$

where (x_i, y_i, z_i) are the known coordinates of sensor P_i, and (x_s, y_s, z_s) are the unknown coordinates of the AE source.

Finally, combining Eqs. (6) and (7) for each triggered sensor yields the system of equations (Eqs. 8–10).

$$\sqrt{(x_2 - x_s)^2 + (y_2 - y_s)^2 + (z_2 - z_s)^2} - \sqrt{(x_1 - x_s)^2 + (y_1 - y_s)^2 + (z_1 - z_s)^2} = v(t_2 - t_1) \tag{8}$$

$$\sqrt{(x_3 - x_s)^2 + (y_3 - y_s)^2 + (z_3 - z_s)^2} - \sqrt{(x_1 - x_s)^2 + (y_1 - y_s)^2 + (z_1 - z_s)^2} = v(t_3 - t_1) \tag{9}$$

$$\sqrt{(x_4 - x_s)^2 + (y_4 - y_s)^2 + (z_4 - z_s)^2} - \sqrt{(x_1 - x_s)^2 + (y_1 - y_s)^2 + (z_1 - z_s)^2} = v(t_4 - t_1) \tag{10}$$

https://doi.org/10.5194/egusphere-2026-5268
Preprint. Discussion started: 9 November 2026
© Author(s) 2026. CC BY 4.0 License.

The unknowns (x_s, y_s, z_s) are then obtained by solving this system of equations.

3 Results

3.1 Flexural strength and effective elastic modulus

The flexural strength obtained from four-point bending tests ranged from 124.6 to 1394.7 kPa with an average of 698.9 ± 361.0 kPa, and the effective elastic modulus varied from 0.5 to 4.2 GPa, averaging 1.8 ± 0.7 GPa. Figure 4 presents the typical history curves of applied force and midspan displacement. During the loading stage, both the applied force and the midspan displacement increased linearly, and the displacements measured by the two LVDTs were nearly identical. At peak load, the specimen failed and the applied force dropped abruptly. Meanwhile, the fractured specimen detached from the supports, causing the displacement recorded by the LVDTs to rise sharply. The location of the main crack between the two loading points was related to the spatial distribution of inherent defects (i.e., brine and gas inclusions) within the specimen. However, owing to the stress concentration beneath the loading points, a higher proportion of specimens exhibited crack initiation exactly at the loading points. Regardless of where the main crack formed, no macroscopic cracks were observed on the specimen surface throughout the entire loading process before sudden failure.

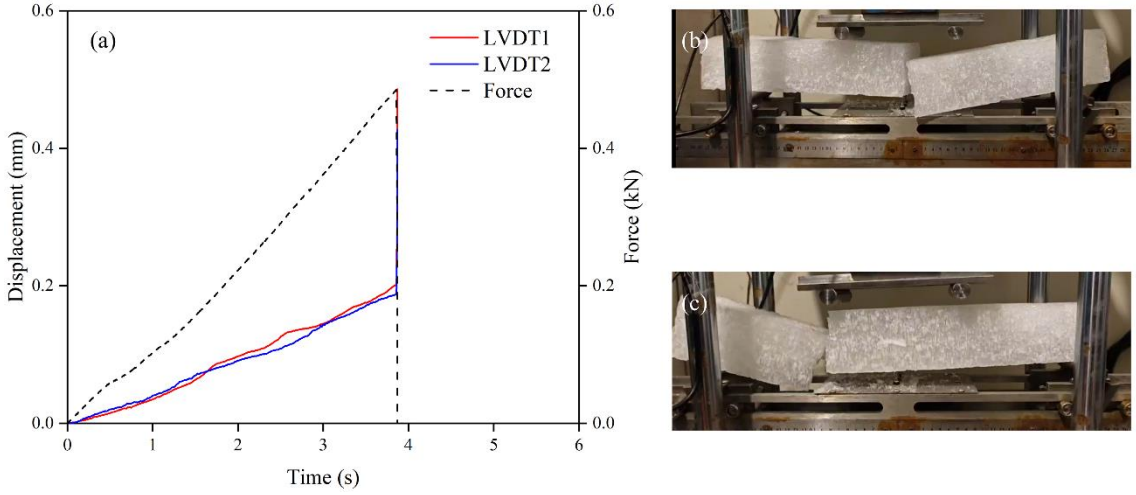


Figure 4: (a) Typical history curves of applied force and midspan displacement, and failed specimen with the main crack (b) between the loading points and (c) beneath a loading point.

Figure 5a presents the box plots of flexural strength varying with respect to ice temperature. Overall, the flexural strength (both mean and median) decreased with increasing temperature. The data exhibited considerable dispersion, with the ratio of the interquartile range (IQR) to the median being at least 80 % at all temperatures except −12 °C. The flexural strength values and the degree of dispersion at −12 °C deviated from this general trend owing to the small sample size ($n = 7$). Excluding the −12 °C data and considering the nonlinear variation of strength as the temperature approaches 0 °C, a logarithmic function was fitted, giving σ_f (kPa) = 162.5ln(|T|) + 431.6, with a coefficient of determination $R^2 = 0.95$ at a significance level of $p < 0.01$.

https://doi.org/10.5194/egusphere-2026-5268
Preprint. Discussion started: 9 November 2026
© Author(s) 2026. CC BY 4.0 License.

Figure 5b shows the box plots of effective elastic modulus as a function of ice temperature. The effective elastic modulus decreased with rising temperature. The modulus also displayed notable dispersion, with the IQR/median ratio ranged from 42 % to 67 % from −12 °C to −6 °C, and the largest ratio (92 %) was observed at −3 °C. Considering the nonlinear behaviour of the modulus near 0 °C, a logarithmic fit was also applied, yielding E (GPa) = 0.26ln(|T|) + 1.31 with R^2 = 0.55 at p = 0.01 level.

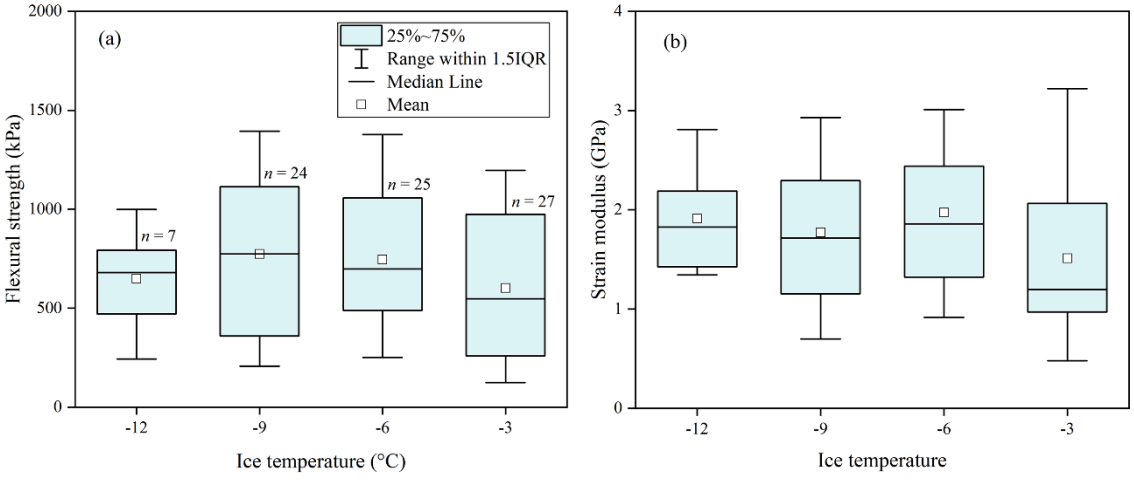


Figure 5: The box plots of (a) flexural strength and (b) effective elastic modulus varying against ice temperature (*n* indicates the sample size at each temperature).

The specimens were derived from sea ice in the summer Arctic, which inherently has low salinity. The salinity was further reduced due to brine drainage during transportation and storage. The specimen salinity ranged from 0 to 3.7 PSU, with a mean of only 0.9 ± 1.0 PSU. The brine volume fraction ranged from 0 to 5%, averaging 1% ± 1%. The drained brine channels were largely occupied by gas, leading to a high gas volume fraction ranging from 1% to 39% and averaging 14% ± 13%. It was found that the flexural strength decreased with increasing gas volume fraction (Fig. 6a). Following the functional form of the flexural strength equation proposed by Timco and O'Brien (1994), an empirical relationship between flexural strength and gas volume fraction was established by fitting the measured data, yielding Eq. (11) with R^2 = 0.64 (p < 0.01).

$$\sigma_f = 1792.2\exp\left(-2.9\sqrt{v_a}\right) \quad (11)$$

where σ_f is in kPa, and v_a is gas volume fraction.

The effective elastic modulus also decreased with increasing gas volume fraction. An empirical equation of the same form as that used for flexural strength was fitted to the measured data, yielding Eq. (12) with R^2 = 0.55 (p < 0.01).

$$E = 3.5\exp\left(-2.1\sqrt{v_a}\right) \quad (12)$$

where E is in GPa.

https://doi.org/10.5194/egusphere-2026-5268
Preprint. Discussion started: 9 November 2026
© Author(s) 2026. CC BY 4.0 License.

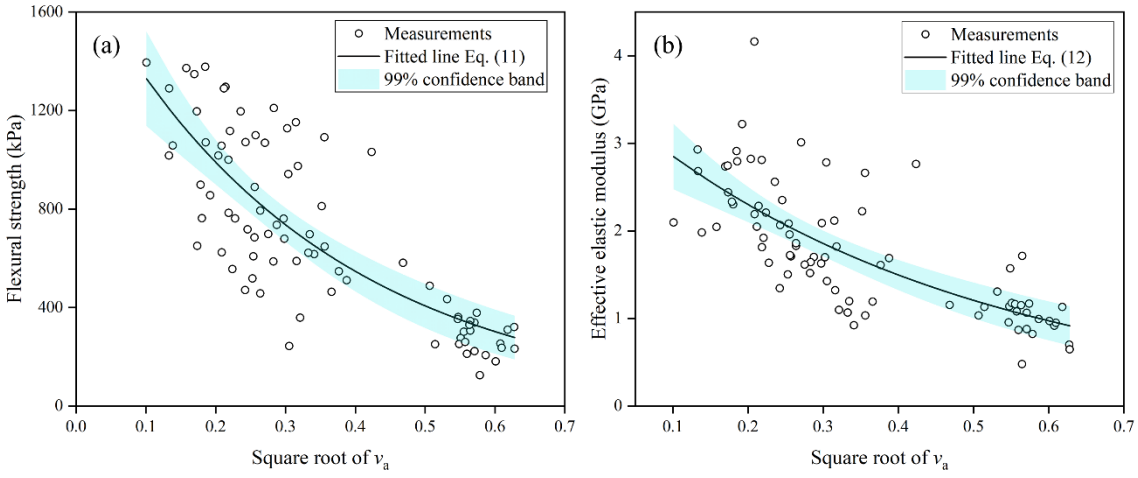


Figure 6: The variations of (a) flexural strength and (b) effective elastic modulus with respect to square root of gas volume fraction.

The flexural strength of low-brine-content (<5%) sea ice specimen in this study was compared with literature data for sea ice of similar brine volume fractions. Timco and Frederking (1983) conducted four-point bending tests on columnar ice at temperatures ranging from −20 °C to −4 °C with brine volume fractions below 5%. They reported a flexural strength of 753.6 ± 210.0 kPa, which is close to the value of 698.9 ± 361.0 kPa obtained in this study. Aly et al (2019) compiled a large dataset of sea ice flexural strength together with corresponding brine volume fractions; from this dataset, data with brine volume fractions comparable to those of the present specimens were selected, yielding an average strength of 872.0 ± 396.7 kPa. Given the inherently high scatter of sea ice strength, this average is also considered comparable to the present measurement. In terms of effective elastic modulus, Karulina et al. (2019) reported field measured values of sea ice effective elastic modulus. Data with brine volume fractions similar to those of our specimens were selected, giving an average modulus of 1.4 ± 0.7 GPa, which is similar to the average value of 1.7 ± 0.7 GPa obtained in the present study.

3.2 Microcracking activity

3.2.1 AE parameters

A total of 4 specimens were conducted using AE monitoring, of which tested at −9 °C was excluded from the below analysis because the wave velocities measured in two orthogonal directions differed substantially. Figure 7 presents the evolution of AE ring-down count and energy during loading. In each subplot, the left panel shows the ring-down count and cumulative ring-down count, and the right panel displays the energy, cumulative energy, and b-value. Since bending failure is sudden and proceeds rapidly, there was a limited number of detectable AE events in each test. Only specimen F2 provided a complete AE record throughout the entire failure process; for the remaining specimens, AE activity was captured only until the main crack initiation stage, after which rapid failure caused poor coupling between sensors and specimen and consequent loss of data

https://doi.org/10.5194/egusphere-2026-5268
Preprint. Discussion started: 9 November 2026
© Author(s) 2026. CC BY 4.0 License.

recording. Nevertheless, it can still be observed that both the ring-down count and the AE energy exhibited an abrupt, order-of-magnitude increase at the onset of the main crack.

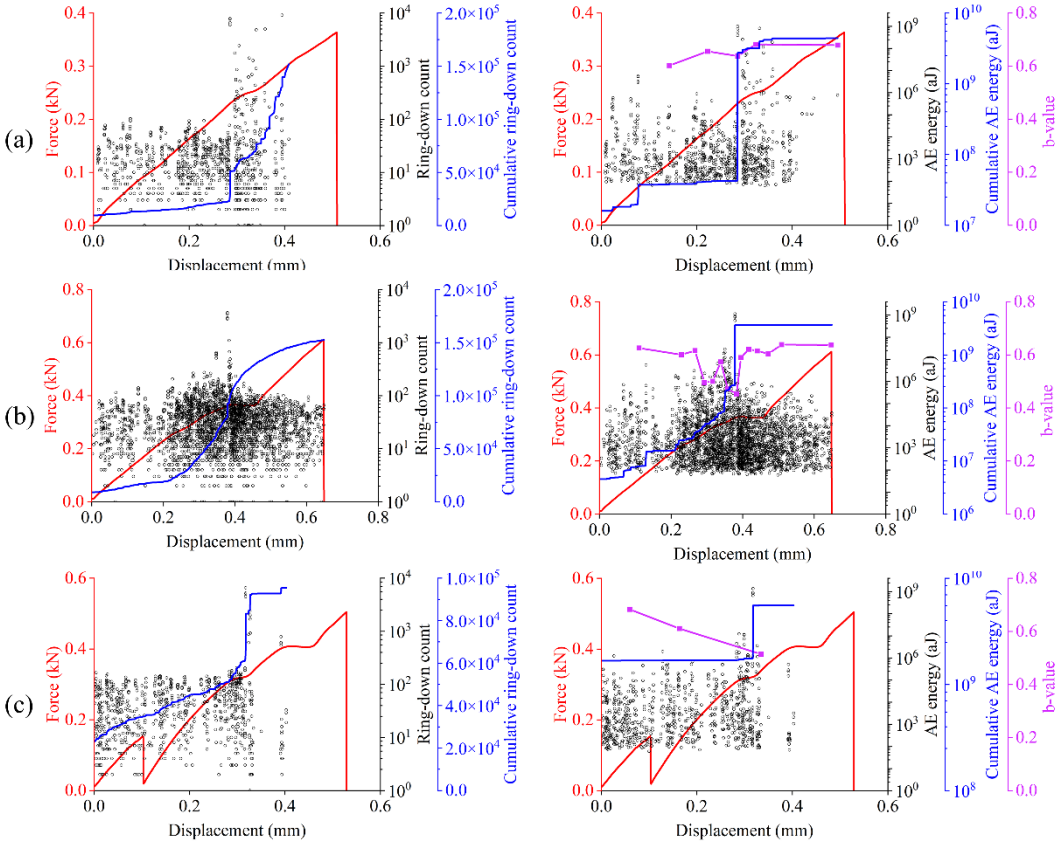


Figure 7: Force–midspan displacement curves, AE ring-down count and energy for the specimens (a) F1, (b) F2, and (c) F3. In each subplot, the left panel shows the ring-down count and cumulative ring-down count, and the right panel shows the AE energy, cumulative energy, and b-value.

Based on the evolution of ring-down count and energy, during the stage before and after main crack initiation, the ring-down counts remained on the order of 10^0–10^2, and the energy fell within the range of 10^2–10^6 aJ. Upon main crack initiation, both the ring-down count and energy exhibited a pronounced rise. The ring-down count increased abruptly to the order of 10^4, and the energy reached 10^9aJ. The abrupt rise was even more obvious in the cumulative ring-down count and cumulative energy. These features indicate that prior to main crack initiation, microcracking within the specimen was mild and associated with low energy release, so that the strain energy was predominantly stored elastically. As the tensile stress at the bottom of the beam increased, originally isolated and stable microcracks coalesced and grew, forming localized dense damage zones that triggered the initiation of a main crack, which was accompanied by high energy release. After the main crack initiated, the opening and sliding of secondary cracks were accompanied by low energy. Subsequently, as the load continued to rise, the main crack propagated rapidly through the entire specimen, ultimately leading to failure. Regarding the b-value evolution, the

https://doi.org/10.5194/egusphere-2026-5268
Preprint. Discussion started: 9 November 2026
© Author(s) 2026. CC BY 4.0 License.

b-value dropped at the moments when the ring-down count and AE energy increased abruptly, reflecting the initiation of large-scale main cracks. Overall, the four-point bending specimens showed b-values between 0.5 and 0.7.

Datt et al. (2020) also reported AE measurements on ice under three-point bending. In their tests with a failure time (2.5 s) comparable to that of the present study, they similarly observed weak AE activity and low energy release during most of the loading period. The AE energy was released predominantly in a burst at the moment of main crack formation, reaching a maximum of approximately 10^8 aJ, which coincided with a pronounced drop in the b-value. Li and Du (2016) also observed that the AE ring-down counts and energy remained at low levels prior to main crack formation in ice bending tests followed by an abrupt increase upon main crack initiation.

To further explore the relationships among AE parameters during bending failure, a cross-parameter correlation analysis was performed using the data from four-point bending specimen F2 (Fig. 8). The parameters analysed were amplitude, centroid frequency, peak frequency, ring-down count, and energy.

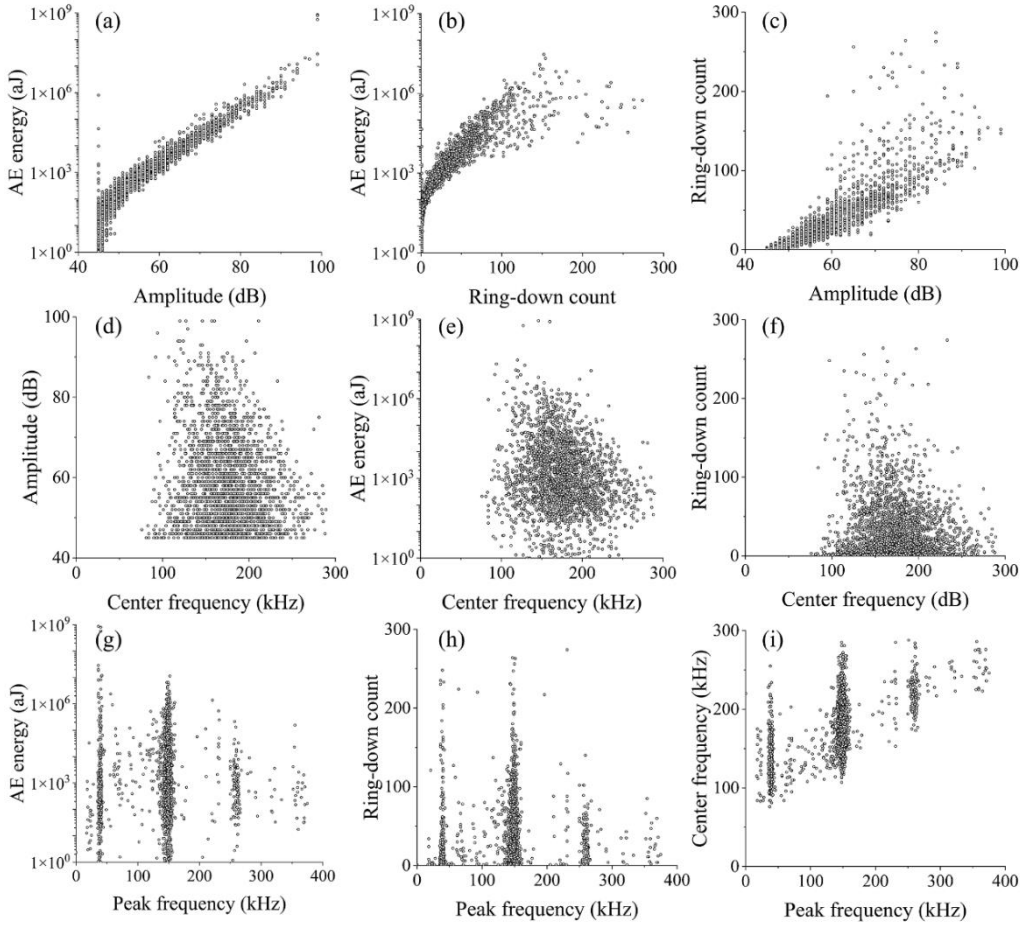


Figure 8: Relationships among AE parameters: (a) amplitude vs. energy, (b) ring-down count vs. energy, (c) amplitude vs. ring-down count, (d) centroid frequency vs. amplitude, (e) centroid frequency vs. energy, (f) centroid frequency vs. ring-down count, (g) peak frequency vs. energy, (h) peak frequency vs. ring-down count, (i) peak frequency vs. centroid frequency.

https://doi.org/10.5194/egusphere-2026-5268
Preprint. Discussion started: 9 November 2026
© Author(s) 2026. CC BY 4.0 License.

Figures 8(a)–(c) present the relationships among amplitude, energy, and ring-down count. These three parameters reflect the instantaneous magnitude, energy release scale, and activity intensity of microcracking, respectively. Overall, these parameters exhibit strong positive correlations. The high-amplitude events are generally accompanied with high energy release and more frequent microcracking activity. The positive relationship between amplitude and ring-down counts was also reported in Datt et al. (2020). It should be noted that the correlated distributions display a broad envelope. For instance, when the amplitude reaches 60 dB and the ring-down count reaches 100, the corresponding energy can vary by at least one order of magnitude. This indicates that, despite the overall positive trend, there is considerable dispersion among the three AE parameters. Amplitude mainly captures the instantaneous peak of the AE signal, whereas energy represents the time-integrated energy of the AE signal over the signal duration. In addition to being influenced by amplitude, the ring-down count is also affected by the signal duration and decay rate. Furthermore, the broad distribution band reflects the intrinsic diversity of AE signals, which arises from variations in microcrack size and type, as well as the heterogeneous distribution of brine pockets and gas bubbles within the sea ice.

Figures 8(d)–(f) present the centroid frequency plotted against amplitude, energy, and ring-down count, respectively. As amplitude, energy, and ring-down count increase, the range of centroid frequency values becomes increasingly narrow. However, the overall scattered distribution indicates that the centroid frequency exhibits no obvious correlation with these three parameters.

Figures 8(g)–(i) show the peak frequency plotted against energy, ring-down count, and centroid frequency, respectively. In the plots of peak frequency vs. energy and ring-down count, two distinct frequency clusters were identified, centred at 38 kHz and 150 kHz, respectively. The 38 kHz cluster spanned a wide range of energy and ring-down counts, indicating that this frequency band contained both low-energy, small-scale microcracking events and high-energy signals released during main crack initiation. The 150 kHz cluster contained the largest number of AE events, corresponding to the majority of microcracking activity. The peak frequency–centroid frequency plot also exhibited these two prominent clusters. Within the 38 kHz cluster, the centroid frequency was higher than the peak frequency, suggesting that the spectral energy was distributed mainly in the mid-to-high frequency range. In the 150 kHz cluster, the peak and centroid frequencies were close, reflecting a concentrated spectral energy distribution and a more stable waveform morphology. In addition, minor AE events also appeared near 250 kHz cluster, but their populations were far smaller than those of the two main frequency clusters.

3.2.2 AE source localization

Since AE source localization relies on the wave velocity, the influence of the measured velocity on the localization results was first assessed. As shown in Figure 9a, the measured velocities ranged from 2636 to 3434 m s^{-1}, which is consistent with previously reported acoustic wave speeds in sea ice (Lishman et al., 2020; Xie and Farmer, 1994). Specimen F3 exhibited the most pronounced velocity anisotropy (2636 vs. 3341 m s^{-1} in two orthogonal directions) and was therefore used as an example to evaluate the effect of wave velocity on AE source localization. In the AE source localization in specimen F3, an average velocity of 2988 m s^{-1} was adopted. Figures 9b and c compares the localization results (X-Z plane) obtained using 2636 m s^{-1}

https://doi.org/10.5194/egusphere-2026-5268
Preprint. Discussion started: 9 November 2026
© Author(s) 2026. CC BY 4.0 License.

and 2988 m s^{-1}. The results show that, compared with the average-velocity case, the AE sources located with the lower velocity were slightly shifted toward the centre of the specimen, whereas the overall spatial distribution pattern remained almost unchanged. The location deviations between the two velocity cases range from 2.7 to 17.7 mm, with a mean of 6.9 ± 3.6 mm. This deviation is negligible relative to the specimen dimensions.

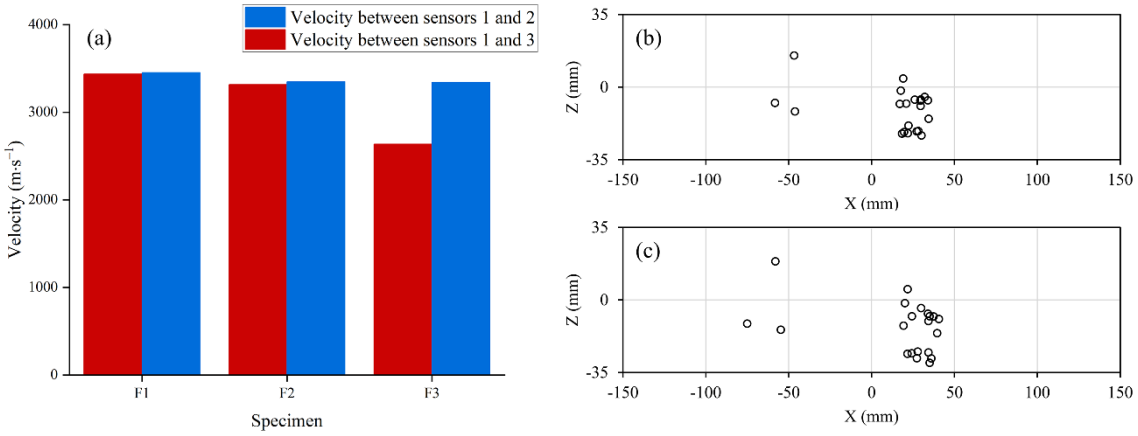


Figure 9: (a) The wave velocity measurements for specimens F1, F2, and F3, and AE source localizations for specimen F3 using velocities of (b) 2636 m s^{-1} and (c) 2988 m s^{-1}.

Figure 10 presents the AE source localization results of microcracks. As mentioned earlier, the AE data of most specimens were lost after main crack initiation; therefore, the microcracks shown in Figure 10 all correspond to the stage up to and including the moment of main crack initiation. It is adequate for the AE activity analysis, as the main crack initiation event was associated with the high energy release, and no high-energy events occurred afterwards. To further examine the spatiotemporal evolution of microcracking, the loading process before main crack initiation was divided into three stages of equal midspan displacement increment. For each stage, the microcrack locations projected onto the X–Z plane and the corresponding AE energy were displayed. Since microcracks occurred only within the central region of specimen, the displayed field is limited to [−150 mm, 150 mm] for clarity.

https://doi.org/10.5194/egusphere-2026-5268
Preprint. Discussion started: 9 November 2026
© Author(s) 2026. CC BY 4.0 License.

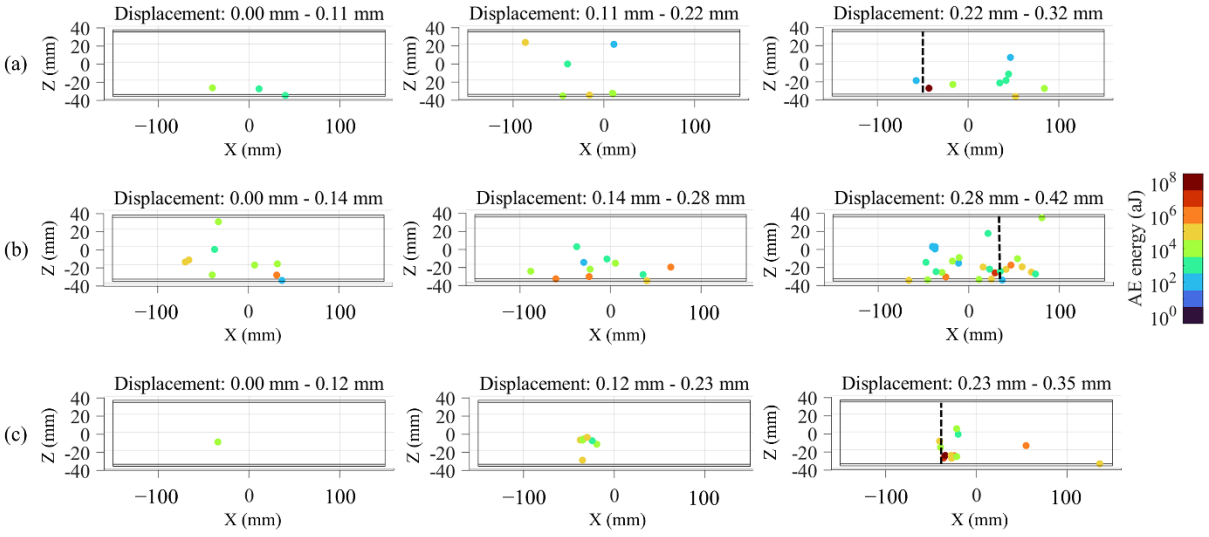


Figure 10: Microcrack locations (X–Z plane) and AE energy for specimens (a) F1, (b) F2, and (c) F3 at three stages of equal midspan displacement increments up to and including main crack initiation. The dashed lines indicate the macroscopic fracture paths.

Regarding the spatial distribution of microcracks, microcracks initially appeared predominantly in the tensile zone at the bottom of the beam and gradually propagated toward the upper-middle region with increasing load. Throughout all stages, microcracks in the upper region remained sparse, with only a few appearing near the loading points due to stress concentration. In contrast, the microcracks in the lower region were distributed over a wider range, extending beyond the pure bending zone into the combined bending and shear zone, covering a longitudinal span of approximately X = [−100 mm, 100 mm]. This occurs because, in the combined bending and shear zone, the superimposed bending normal stress and shear stress cause the principal tensile stress to deviate from the horizontal direction, leading to the formation of inclined cracks and an outward expansion of the damage zone along the bottom of the beam.

During the early loading stage, the AE energy of microcracks was mainly concentrated in the range of 10^2–10^6 aJ, and the AE events in the lower part of the specimen generally exhibited higher energy, indicating that the tensile stress in that region dominated the microcrack damage. At the stage immediate before main crack initiation, all specimens generated high-energy microcracks with energies exceeding 10^7 aJ, and the locations of these high-energy microcracks coincided with the eventual macroscopic fracture paths. Taking specimen F1 as an example, the high-energy microcrack with an energy of 10^8 aJ appeared at X = 40 mm just before main crack initiation. Although a greater number of low-energy damage events were clustered around X ≈ −50 mm on the opposite side, the final fracture path still developed at the site of this high-energy microcrack. This phenomenon suggests that macroscopic fracture of the specimen is not governed by the accumulation of microcrack density, but rather by a local microcrack that first reaches the critical condition for unstable propagation. This is consistent with the view of Schulson (2001) that sea ice brittle failure is determined not by the number of cracks, but by whether a crack propagates to form an unstable structure.

https://doi.org/10.5194/egusphere-2026-5268
Preprint. Discussion started: 9 November 2026
© Author(s) 2026. CC BY 4.0 License.

4 Discussion

4.1 A two-variable model estimating sea ice flexural strength

The sea ice flexural strength is commonly estimated using the empirical formula proposed by Timco and O'Brien (1994), which takes the brine volume fraction as the variable. However, this formula is applicable to sea ice in the growth season. For warm sea ice in the melt season, brine is substantially drained and the vacated brine channels become occupied by gas, leading to a significant overestimation of flexural strength if the formula is still applied. Comparison shows that the strengths calculated using the Timco and O'Brien formula are approximately 190 kPa in average higher than the measured values of low-brine-content specimens in this study. Therefore, developing a flexural strength calculation method suitable for sea ice in both the growth and melt seasons has become a critical issue that needs to be addressed.

Given the difference in the mechanical properties between gas (compressible) and brine (incompressible), gas bubbles are essentially voids that cannot transmit force, whereas brine pockets are filled with fluid that can transmit pressure. Moreover, the bond strength at the brine pockets–ice grains interface is weak. The formula proposed by Timco and O'Brien (1994) can be regarded as describing the dependence of flexural strength on brine volume fraction, and the empirical equation (Eq. 11) proposed in this study can be regarded as describing the dependence on gas volume fraction. Therefore, the brine and gas volume fractions are adopted as two variables to establish a formula to estimate the sea ice flexural strength.

Available studies that report the sea ice flexural strength along with both the brine and gas volume fractions are limited. A combined dataset was compiled here from the experimental results obtained in this study and the author's previous work, comprising a total of 205 specimens. This dataset includes four- and three-point bending tests as well as cantilever beam tests. The brine volume fractions of the specimens range from 0 to 0.19, and the gas volume fractions from 0 to 0.39.

Table 3: Information on the data used for fitting Eqs. (13) and (14). v_a and v_b indicate gas and brine volume fractions.

Data source	Test type	v_b	v_a	σ_f (kPa)	E (GPa)
Xiu et al. (2022)	3-point bending	0.01–0.04	0.001–0.1	540–1480	0.2–5.1
Wang et al. (2022)	3-point bending	0.01–0.06	0.03–0.12	305–1120	0.4–2.3
Wang et al. (2025)	3-point bending	0–0.02	0.03–0.18	570–1148	1.6–6.6
This study	4-point bending	0–0.05	0–0.39	124–1394	0.5–4.2
Bohai sea ice	3-point bending	0.03–0.19	0.01–0.08	143–836	0.3–2.7
	Cantilever beam	0.11–0.16	0.02–0.13	222–470	0.5–3.3

Using the data presented in Table 3, an empirical equation Eq. (13) for the sea ice flexural strength was obtained as a function of brine and gas volume fractions with $R^2 = 0.61$ ($p < 0.01$). Figure 11 further shows the variation of flexural strength with brine and gas volume fractions.

https://doi.org/10.5194/egusphere-2026-5268
Preprint. Discussion started: 9 November 2026
© Author(s) 2026. CC BY 4.0 License.

$$\sigma_f = 2225.6\exp(-2.5\sqrt{v_b} - 2.9\sqrt{v_a}) \quad (13)$$

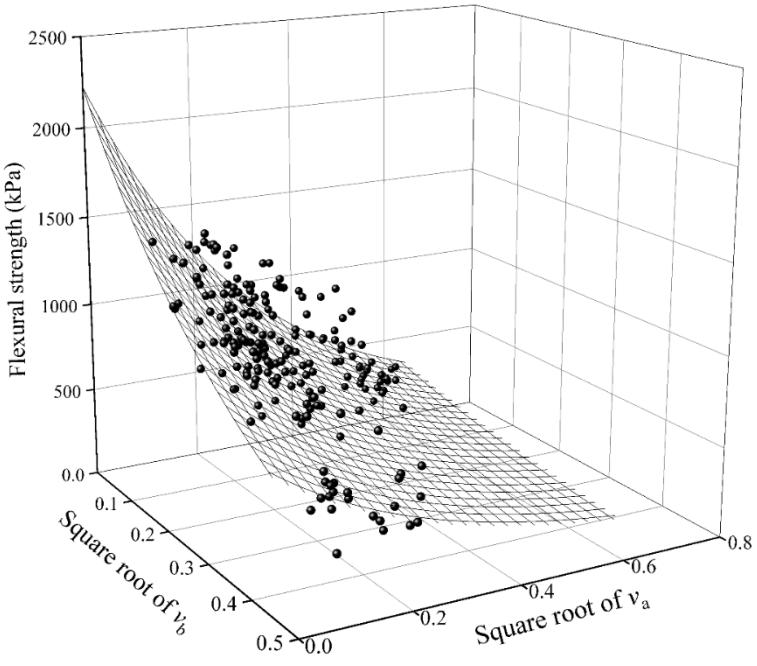


Figure 11: The variation of sea ice flexural strength with brine and gas volume fractions

It is noteworthy that when the two-variable exponential model was extended to the effective elastic modulus and fitted to the data in Table 3, the resulting empirical equation $E = 4.4\exp(-2.2\sqrt{v_b} - 1.8\sqrt{v_a})$ yielded only R^2 = 0.21 (p < 0.01), which is substantially lower than that obtained for flexural strength. This suggests that the flexural strength of sea ice is primarily governed by the content of brine and gas inclusions, and can therefore be described by a simple function of brine and gas volume fractions. In contrast, the effective elastic modulus is a small-strain stiffness and therefore depends more strongly on the microstructural characteristics of ice grain. Our previous study found that the effective elastic modulus is closely related to the ice platelet spacing rather than to brine and gas contents (Wang et al., 2022). Hence, accurately calculating the effective elastic modulus of sea ice requires additional microstructural parameters.

It should be acknowledged that the applicability of the two-variable model for sea ice flexural strength proposed here still requires validation with additional experimental data. In particular, the current database lacks specimens with high brine volume fractions. Most of the data listed in Table 3 were obtained from ice collected in the polar regions and subjected to prolonged storage during transportation, during which substantial brine drainage occurred, resulting in low brine volume fractions. Therefore, future efforts should focus on in-situ mechanical testing or prompt testing shortly after ice sampling to improve the robustness of the model.

https://doi.org/10.5194/egusphere-2026-5268
Preprint. Discussion started: 9 November 2026
© Author(s) 2026. CC BY 4.0 License.

4.2 High-energy microcracks

The results presented in Sect. 3.2.2 showed that at the stage immediate before main crack initiation, all specimens generated high energy microcracks with energies exceeding 10^7 aJ, and the locations of these high energy events coincided with the eventual macroscopic fracture paths, suggesting that they triggered the ultimate failure of the specimens. To further investigate the underlying mechanisms, the AE signals corresponding to these high-energy microcracks were analysed. Figure 12 shows the time-domain waveform, the frequency-domain spectrum (after FFT), and the time-frequency plot (after wavelet transform) of the AE signals associated with the high-energy microcracks for each specimen. The time-domain waveforms reflect the amplitude variations of the signals, the FFT spectrum reveal the dominant frequency components, and the wavelet time-frequency plots depict the temporal evolution of the frequency components.

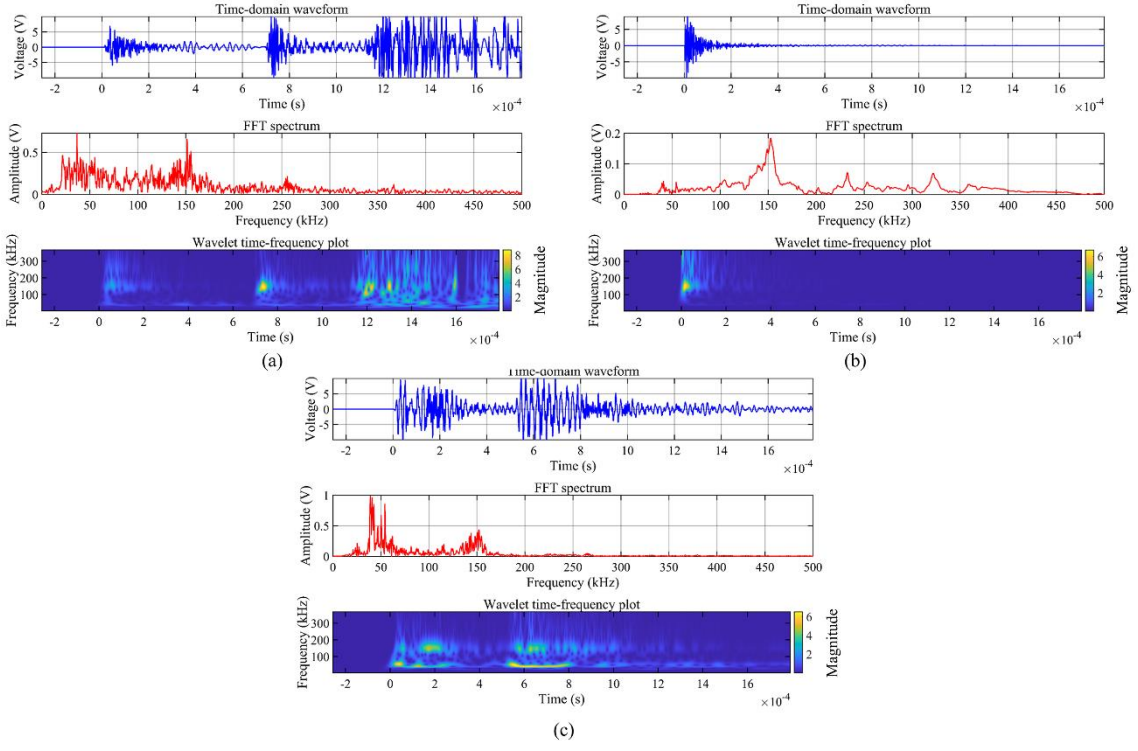


Figure 12: Time-domain waveforms, FFT spectrum, and time-frequency plots of the AE signals corresponding to the high-energy microcracks in specimens (a) F1, (b) F2, and (c) F3. The negative time values on the time axis result from the 256 μs pre-trigger setting.

It should be noted that AE source localization typically treats AE sources as point sources and assumes that AE sources are temporally separated. However, an AE event actually may comprise signals from multiple microcracking activities, which are merged in post-processing and treated as the event first captured by the sensors. As can be observed from the time-domain waveforms, specimen F2 exhibited a single pulse, corresponding to an individual microcracking event, whereas the signals from the other specimens were of longer duration and displayed distinct multiple oscillations and energy releases, indicating the superposition of multiple microcracking activities. This observation is corroborated by previous findings on crack

https://doi.org/10.5194/egusphere-2026-5268
Preprint. Discussion started: 9 November 2026
© Author(s) 2026. CC BY 4.0 License.

propagation in saline ice. Petrenko and Gluschenkov (1996) and Arakawa and Petrenko (2003) demonstrated that cracks in saline ice propagate in a discontinuous, jump-and-arrest manner, owing to the interaction between the crack tip and brine inclusions. As a crack encounters these liquid inclusions, it is temporarily arrested; upon further loading, it reinitiates and jumps to the next obstacle, generating a series of discrete cracking events within a short time interval. DeFranco and Dempsey (1994) further characterized this behaviour as stick-slip cracking in saline ice, in which repeated initiation-arrest cycles occur under increasing load. Each cycle corresponds to a distinct microcracking event.

Based on the underlying mechanism of acoustic emission, the frequency of the elastic wave radiated by a microcrack is inversely proportional to the crack size and proportional to the wave velocity (Brune, 1970). For specimen F1, the FFT spectrum displays a broadband characteristic with two distinct peaks at 38 kHz and 150 kHz. The time-domain waveform can be separated into three successive AE events. The first and second events are of short duration, with energy concentrated around 150 kHz, as shown in the time-frequency plot. The 150 kHz component lies in the mid-to-high frequency band and is typically associated with small-scale microcracks, indicating isolated microcrack nucleation. The third event exhibits a longer duration, with energy concentrated at both 150 kHz and 38 kHz but dominated by the 150 kHz component. The 150 kHz contribution reflects the nucleation of continuous small-scale microcracks; whereas the 38 kHz component belongs to the low-frequency range and corresponds to larger-scale microcracks, suggesting that persistent friction, sliding, and coalescence among small microcracks led to the formation of larger microcracks.

For specimen F2, the AE signal is of short duration with energy concentrated at 150 kHz, indicating a single isolated microcrack nucleation. Notably, this single event directly triggered the final failure of the specimen, suggesting that a violent microcracking at this location caused an instantaneous and substantial release of local stress, thereby acting as the critical source for main crack initiation.

For specimen F3, the recorded AE event exhibits a long duration, with energy concentrated at 38 kHz, corresponding to the formation of larger-scale microcracks generated by continuous friction, sliding, and coalescence among small microcracks.

In summary, while all specimens ultimately failed by a high-energy microcracking event that served as the critical source for main crack initiation, two distinct micromechanical pathways can be identified. The first is characterized by a high-frequency signal, corresponding to an isolated microcrack directly triggered failure without additional events resolved in the AE record. In contrast, the second is characterized by a low-frequency signal containing multiple successive AE events, indicating that the final failure was preceded by a rapid cascade of microcracking activities that merged into a larger microcrack, including friction, sliding, and coalescence among small microcracks. This difference can be attributed to the local microstructural heterogeneity of sea ice. The brine and gas inclusions act as inherent defects within sea ice. In regions with uniformly distributed defects, stress is released through progressive linkage of distributed damage; whereas when a single defect acts as a dominant stress concentrator, failure can be triggered by its extension alone. These findings demonstrate that the AE signal characteristics not only serve as the precursors to failure but also provide information on the underlying microcrack evolution, which governs the macroscopic failure behaviour of sea ice under bending.

https://doi.org/10.5194/egusphere-2026-5268
Preprint. Discussion started: 9 November 2026
© Author(s) 2026. CC BY 4.0 License.

4.3 Influence of sea ice inclusions on microcracking activity

Li and Du (2016) reported AE monitoring results from three-point bending tests on artificially frozen freshwater ice, and identified three peak frequency clusters centred at 30–50 kHz, 150–180 kHz, and 240–250 kHz, respectively. This finding is consistent with the peak frequency distribution observed in the present study, where three clusters were identified at 38 kHz, 150 kHz, and 250 kHz. A comparison with the results of Li and Du (2016) shows that the 150 kHz cluster dominates the bending failure of both freshwater and sea ice. As discussed in Sect. 4.2, under flexural loading, the AE signal with energy concentrated at 150 kHz corresponds to the formation of a single crack event. According to Schulson (2001), such an event typically signifies the formation of a parent crack during the brittle failure in ice. In freshwater ice, parent cracks predominantly initiate from grain boundary fractures; in sea ice, however, due to the weak bonding at the interface between ice grains and brine pockets, parent cracks tend to preferentially initiate along these weak boundaries.

Notably, compared with the freshwater ice bending tests of Li and Du (2016), the present sea ice bending tests exhibit a significantly higher proportion of low-frequency (~38 kHz) signals. Li and Du (2016) also conducted AE monitoring on freshwater ice under uniaxial compression and found that low-frequency (30–50 kHz) signals dominated the compressive failure, which they attributed to the formation of comb cracks. According to Schulson (2001), comb cracks arise from frictional sliding and shear instability along parent crack surfaces. This is consistent with our interpretation of the 38 kHz cluster as representing the persistent friction, sliding, and coalescence among microcracks.

Why are low-frequency signals more prominent in the bending failure of sea ice? The difference can be explained by the complex microstructure of sea ice, which affects crack nucleation and propagation. The brine pockets within sea ice act as preferential sites for stress concentration under external loading and promote microcrack initiation (Picu et al., 1994). Once a parent crack forms, its propagation is not continuous; rather, it involves frequent interactions with brine inclusions, exhibiting intermittent stick-slip behaviour (DeFranco and Dempsey, 1994). This discontinuous propagation breaks a single crack event into a series of discrete micro-rupture events, which naturally correspond to lower frequency components in the frequency domain, as confirmed by Figs. 12a and c. Moreover, the arrest phase following each jump requires an increase in external load to restart the crack. During this period, frictional sliding occurs between the crack faces, and the resulting stick-slip behaviour itself serves as a source of low-frequency waveform. In addition, the presence of brine pockets not only makes the crack propagation path highly tortuous (Arakawa and Petrenko, 2003) but also enhances friction and interlocking effects during crack-face sliding, further concentrating the energy release in the low-frequency band. Therefore, the pronounced low-frequency signals observed in the bending failure of sea ice result from the combined effects of discontinuous crack propagation, frictional sliding of crack faces, and tortuous crack paths.

The influence of microstructural heterogeneity of sea ice on its microcracking activity is also reflected in the b-value. In the bending tests of Li and Du (2016), the initial b-value exceeded 1.1 and dropped to 0.5–0.6 at main crack initiation. Datt et al. (2020) reported an initial b-value of approximately 1.0 in freshwater ice bending, which decreased to about 0.4 at main crack initiation. In contrast, the overall b-value in the present study ranged between 0.5 and 0.7, with an initially low value that

https://doi.org/10.5194/egusphere-2026-5268
Preprint. Discussion started: 9 November 2026
© Author(s) 2026. CC BY 4.0 License.



further decreased to approximately 0.4 at main crack initiation. This marked discrepancy arises because the brine pockets and gas bubbles act as inherent defects within sea ice. At the early stage of loading, these defects promote microcracks of larger scale compared to those in freshwater ice, resulting in a lower initial b-value and a higher proportion of large-scale cracking event throughout the entire loading process.

5 Conclusions

Four-point bending tests were performed in the cold laboratory using beam specimens machined from sea ice collected in the Arctic Ocean during summer. As a result of brine drainage, the gas content was higher than the brine content within the ice. The flexural strength and effective elastic modulus of sea ice were determined from the mechanical tests. Meanwhile, four AE sensors were mounted on the four surfaces of ice specimens to monitor the microcracking activity throughout the loading process.

The flexural strength ranged from 124.6 to 1394.7 kPa, averaging 698.9 ± 361.0 kPa, and the effective elastic modulus varied from 0.5 to 4.2 GPa, averaging 1.8 ± 0.7 GPa. These values are comparable to previously reported data for low-brine-content sea ice. Both the flexural strength and the effective elastic modulus decrease with increasing ice temperature and gas volume fraction. A dataset comprising 205 measurements of flexural strength along with brine and gas volume fractions was compiled. Based on this dataset, an empirical equation for sea ice flexural strength was established using brine and gas volume fractions as two independent variables. This two-variable model is applicable to sea ice in both the growth and melt seasons, overcoming the limitation of the conventional formula based solely on brine volume fraction, which is unsuitable for melting sea ice.

AE analysis reveals that during the bending failure of sea ice, microcracking activity prior to main crack initiation is weak. At main crack initiation, both the ring-down count and AE energy increase abruptly. The catastrophic failure of sea ice is governed not by the progressive accumulation of microcrack density, but by a local high-energy microcrack that first reaches the critical condition for unstable propagation. Two typical AE signal modes were identified during bending failure, namely a high-frequency mode (~150 kHz) corresponding to the nucleation of an isolated parent microcrack, and a low-frequency mode (~38 kHz) reflecting friction and sliding among secondary microcracks. Compared with freshwater ice, sea ice exhibits a higher proportion of low-frequency AE signals, which is attributed to the combined effects of discontinuous crack propagation, frictional sliding of crack faces, and tortuous crack paths induced by the presence of brine inclusions.

It should be noted that the applicability of the two-variable model for sea ice flexural strength requires further validation, as the current dataset consists predominantly of low-brine-content sea ice specimens. Future work should include in-situ mechanical measurements to expand the range of brine and gas volume fractions and improve the robustness of the model. In addition, because sea ice bending failure proceeds rapidly, it remains challenging to capture complete AE signals throughout the entire process. Therefore, further bending tests combined AE monitoring are needed to provide a more comprehensive understanding of microcrack evolution mechanisms.

https://doi.org/10.5194/egusphere-2026-5268
Preprint. Discussion started: 9 November 2026
© Author(s) 2026. CC BY 4.0 License.

Data availability

All data are available at the website (https://doi.org/10.5281/zenodo.21866754).

Author contribution

Conceptualization: QW; Investigation: JL, KL and XZL; Formal analysis: QW, KL, ZL; Writing (original draft preparation): QW and JL; Writing (review and editing): PL and JZL.

Competing interests

The authors declare that they have no conflict of interest.

Acknowledgement

This research was supported by the National Natural Science Foundation of China (42676307, 42276242, 52192692, and 42320104004), and the Liaoning Provincial Joint Science and Technology Plan Project (2024JH2/102600012).

References

Aly, M., Taylor, R., Bailey-Dudley, E., and Turnbull, I.: Scale effect in ice flexural strength, J. Offshore Mech. Arct. Eng., 141(5), 051501, https://doi.org/10.1115/1.4042388, 2019.

Arakawa, M. and Petrenko, V. F.: Observation of crack propagation in saline ice and freshwater ice with fluid inclusion, Can. J. Phys., 81(1–2), 159–166, https://doi.org/10.1139/p03-021, 2003.

ASTM International: Standard terminology for nondestructive examinations, ASTM E1316-25, ASTM International, West Conshohocken, PA, USA, https://doi.org/10.1520/E1316-25, 2025.

Barrette, P. D.: A laboratory study on the flexural strength of white ice and clear ice from the Rideau Canal skateway, Can. J. Civ. Eng., 38(12), 1435–1439, https://doi.org/10.1139/L11-106, 2011.

Blanchet, D., Abdelnour, R., and Comfort, G.: Mechanical properties of first-year sea ice at Tarsiut Island, J. Cold Reg. Eng., 11(1), 59–83, https://doi.org/ 10.1061/(ASCE)0887-381X(1997)11:1(59), 1997.

Boniface, A., Saliba, J., Sbarta ï Z. M., Ranaivomanana, N., Balayssac, J. P.: Evaluation of the acoustic emission 3D localisation accuracy for the mechanical damage monitoring in concrete, Eng. Fract. Mech., 223, 106742, https://doi.org/10.1016/j.engfracmech.2019.106742, 2020.

Brune, J. N.: Tectonic stress and the spectra of seismic shear waves from earthquakes, J. Geophys. Res., 75(26), 4997–5009, 1970.

https://doi.org/10.5194/egusphere-2026-5268
Preprint. Discussion started: 9 November 2026
© Author(s) 2026. CC BY 4.0 License.

Cox, G. F. N. and Weeks, W. F.: Equations for determining the gas and brine volumes in sea ice samples, J. Glaciol., 29(102), 306–316, https://doi.org/10.1017/ S0022143000008364, 1983.

Datt, P., Chandel, C., Kumar, V., Sheoran, R., Nasker, D., Kapil, J. C., Srivastava, P. K.: Analysis of acoustic emission characteristics of ice under three point bending, Cold Reg. Sci. Technol., 174, 103063, https://doi.org/10.1016/j.coldregions.2020.103063, 2020.

DeFranco, S. J. and Dempsey, J. P.: Crack propagation and fracture resistance in saline ice, J. Glaciol., 40(136), 451–462, https://doi.org/ 10.1017/S0022143000012326, 1994.

Edington, D., Murdza, A., and Schulson, E. M.: Increasing the flexural strength of columnar-grained ice by an icy coating, J. Glaciol., 71, e90, 1–5, https://doi.org/10.1017/jog.2025.10077, 2025.

Frost, H. J.: Mechanisms of crack nucleation in ice, Eng. Fract. Mech., 68(17–18), 1823–1837, https://doi.org/ 10.1016/S0013-7944(01)00036-4, 2001.

Gold, L. W.: The cracking activity in ice during creep, Can. J. Phys., 38(9),1137–1148. https://doi.org/10.1139/p60-122, 1960.

Karulina, M., Marchenko, A., Karulin, E., Sodhi, D., Sakharov, A., and Chistyakov, P.: Full-scale flexural strength of sea ice and freshwater ice in Spitsbergen Fjords and North-West Barents Sea, Appl. Ocean Res., 90, 101853, https://doi.org/10.1016/j.apor.2019.101853, 2019.

Kolari, K.: Modeling splitting and spalling of columnar ice compressed biaxially: The role of crack nucleation, J. Geophys. Res.-Solid Earth, 124(4), 3271–3287, https://doi.org/10.1029/2018JB017032, 2019.

Li, D. and Du, F.: Monitoring and evaluating the failure behavior of ice structure using the acoustic emission technique, Cold Reg. Sci. Technol., 129, 51–59, https://dx.doi.org/10.1016/j.coldregions.2016.06.003, 2016.

Lishman, B., Marchenko, A., Sammonds, P., and Murdza, A.: Acoustic emissions from in situ compression and indentation experiments on sea ice, Cold Reg. Sci. Technol., 172, 102987, https://doi.org/10.1016/j.coldregions.2019.102987, 2020.

Liu, X., Han, M., He, W., Li, X., and Chen, D.: A new b Value estimation method in rock acoustic emission testing, J. Geophys. Res.-Solid Earth, 125(12), e2020JB019658, https://doi.org/10.1029/2020jb019658, 2020.

Moradian, Z., Einstein, H. H., and Ballivy, G.: Detection of cracking levels in brittle rocks by parametric analysis of the acoustic emission signals, Rock Mech. Rock Eng., 49(3), 785–800, https://doi.org/10.1007/s00603-015-0775-1, 2016.

Ohno, K. and Ohtsu, M.: Crack classification in concrete based on acoustic emission, Constr. Build Mater., 24(12), 2339–2346, https://doi.org/10.1016/j.conbuildmat.2010.05.004, 2010.

Petrenko, V. F. and Gluschenkov, O.: Crack velocities in freshwater and saline ice, J. Geophys. Res.-Solid Earth, 101(B5), 11541–11551, https://doi.org/10.1029/96JB00533, 1996.

Picu, R. C., Gupta, V., and Frost, H. J.: Crack nucleation mechanism in saline ice, J. Geophys. Res.-Solid Earth, 99(B6), 11775–11786, https://doi.org/10.1029/94JB00685, 1994.

Roberts, N. S., Bell, A. F., and Main, I. G.: Are volcanic seismic b-values high, and if so when? J. Volcanol. Geoth. Res., 308, 127–141, https://doi.org/10.1016/j. jvolgeores.2015.10.021, 2015.

https://doi.org/10.5194/egusphere-2026-5268
Preprint. Discussion started: 9 November 2026
© Author(s) 2026. CC BY 4.0 License.



Schulson, E. M.: Brittle failure of ice, Eng. Fract. Mech., 68(17–18), 1839–1887, https://doi.org/ 10.1016/S0013-7944(01)00037-6, 2001.

Sinha, N. K.: Acoustic emission and microcracking in ice, in Proceedings of the 1982 Joint Conference on Experimental Mechanics, Society of Experimental Stress Analysis/Japan Society for Mechanical Engineers, Honolulu/Maui, Hawaii, 23–28 May 1982.

Taylor, R., Turnbull, I., Bailey-Dudley, E., and Pritchett, R.: Full-scale in-situ four-point bending field tests on sea ice, in Proceedings of the ASME 2021 40th International Conference on Ocean, Offshore and Arctic Engineering (OMAE2021), Fort Lauderdale, Florida, 21–30 June 2021.

Timco, G. W. and Frederking, R. M. W.: Flexural strength and fracture toughness of sea ice, Cold Reg. Sci. Technol., 8(1), 35–41, https://doi.org/ 10.1016/0165-232X(83)90015-0, 1983.

Timco, G. W. and O'Brien, S.: Flexural strength equation for sea ice, Cold Reg. Sci. Technol., 22(3), 285–298, https://doi.org/10.1016/0165-232X(94)90006-X, 1994.

Timco, G. W. and Weeks, W. F.: A review of the engineering properties of sea ice, Cold Reg. Sci. Technol., 60(2), 107–129, https://doi.org/10.1016/j.coldregions.2009.10.003, 2010.

Wang, Q., Li, Z., Lu, P., Xu, Y., and Li, Z.: Flexural and compressive strength of the landfast sea ice in the Prydz Bay, East Antarctic, The Cryosphere, 16(5), 1941–1961, https://doi.org/10.5194/tc-16-1941-2022, 2022.

Wang, Q., Liu, K., Lepparänta, M., Cheng, B., Huo, L., Liu, Y., Lu, P., and Li, Z.: Microcrack evolution and damage mechanisms of natural ice under ductile compressive strain revealed by acoustic emission, Eng. Fract. Mech., 336, 111949, https://doi.org/10.1016/j.engfracmech.2026.111949, 2026.

Wang, Q., Liu, K., and Li, Z.: Four-point bending and AE data of sea ice, Zenodo [data set], https://doi.org/10.5281/zenodo.21866754, 2026.

Wang, Q., Liu, Y., Lu, P., and Li, Z.: The mechanical properties of gas-enriched sea ice, Cold Reg. Sci. Technol., 239, 104576, https://doi.org/10.1016/j.coldregions.2025.104576, 2025.

Weiss, J. and Grasso, J. R.: Acoustic emission in single crystals of ice, J. Phys. Chem. B, 101(32), 6113–6117, https://doi.org/10.1021/jp963157f, 1997.

Xie, Y. and Farmer, D. M.: Seismic-acoustic sensing of sea ice wave mechanical properties, J. Geophys. Res.-Oceans, 99(C4), 7771–7786, https://doi.org/10.1029/ 93JC03483, 1994.

Xiu, Y., Li, Z., Wang, Q., Han, H., Zong, Z., Zu, Y., and Zhang, Y.: Experimental study on flexural strength and effective elastic modulus of granular ice in the Bohai Sea, China, Front. Energy Res., 10, 970051, https://doi.org/10.3389/fenrg.2022.970051, 2022.